Chinese Pharmaceutical Association
Institute of Materia Medica, Chinese Academy of Medical Sciences

Acta Pharmaceutica Sinica B

www.elsevier.com/locate/apsb
www.sciencedirect.com

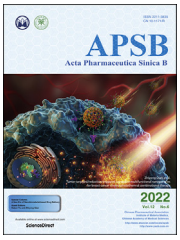

ORIGINAL ARTICLE

Enzyme-instructed and mitochondria-targeting peptide self-assembly to efficiently induce immunogenic cell death

Debin Zheng[a], Jingfei Liu[a], Limin Xie[a], Yuhan Wang[a], Yinghao Ding[b], Rong Peng[a], Min Cui[c], Ling Wang[b], Yongjie Zhang[c,*], Chunqiu Zhang[a,*], Zhimou Yang[a,*]

[a]*Key Laboratory of Bioactive Materials, Ministry of Education, State Key Laboratory of Medicinal Chemical Biology, College of Life Sciences, Collaborative Innovation Center of Chemical Science and Engineering, National Institute of Functional Materials, Nankai University, Tianjin 300071, China*
[b]*College of Pharmacy, Nankai University, Tianjin 300071, China*
[c]*Department of Human Anatomy, Nanjing Medical University, Nanjing 211166, China*

Received 7 May 2021; received in revised form 2 June 2021; accepted 29 June 2021

KEY WORDS

Immunogenic cell death;
Self-assembly;
Mitochondria targeting;
Enzyme

Abstract Immunogenic cell death (ICD) plays a major role in cancer immunotherapy by stimulating specific T cell responses and restoring the antitumor immune system. However, effective type II ICD inducers without biotoxicity are still very limited. Herein, a tentative drug- or photosensitizer-free strategy was developed by employing enzymatic self-assembly of the peptide F-pY-T to induce mitochondrial oxidative stress in cancer cells. Upon dephosphorylation catalyzed by alkaline phosphatase overexpressed on cancer cells, the peptide F-pY-T self-assembled to form nanoparticles, which were subsequently internalized. These affected the morphology of mitochondria and induced serious reactive oxygen species production, causing the ICD characterized by the release of danger-associated molecular patterns (DAMPs). DAMPs enhanced specific immune responses by promoting the maturation of DCs and the intratumoral infiltration of tumor-specific T cells to eradicate tumor cells. The dramatic immunotherapeutic capacity could be enhanced further by combination therapy of F-pY-T and anti-PD-L1 agents without visible biotoxicity in the main organs. Thus, our results revealed an alternative strategy to induce efficient ICD by physically promoting mitochondrial oxidative stress.

© 2022 Chinese Pharmaceutical Association and Institute of Materia Medica, Chinese Academy of Medical Sciences. Production and hosting by Elsevier B.V. This is an open access article under the CC BY-NC-ND license (http://creativecommons.org/licenses/by-nc-nd/4.0/).

*Corresponding authors. Tel./fax: +86 25 86869485 (Yongjie Zhang); +86 22 23502875 (Chunqiu Zhang and Zhimou Yang).
E-mail addresses: zhangyongjie@njmu.edu.cn (Yongjie Zhang), zhangcq@nankai.edu.cn (Chunqiu Zhang), yangzm@nankai.edu.cn (Zhimou Yang).
Peer review under responsibility of Chinese Pharmaceutical Association and Institute of Materia Medica, Chinese Academy of Medical Sciences.

https://doi.org/10.1016/j.apsb.2021.07.005
2211-3835 © 2022 Chinese Pharmaceutical Association and Institute of Materia Medica, Chinese Academy of Medical Sciences. Production and hosting by Elsevier B.V. This is an open access article under the CC BY-NC-ND license (http://creativecommons.org/licenses/by-nc-nd/4.0/).

1. Introduction

Immunotherapy has been broadly considered a promising therapeutic modality for cancer treatment. Immune checkpoint blockade (ICB) therapy exhibited enormous potential for the treatment of malignant tumors[1]. However, tumor cells inherently have resistance to cell death and the ability to escape immune eradication, resulting to less than 20% to 40% of patients benefiting from ICB therapy[2−4]. Therefore, activating the dysfunctional antitumor immune system and reconstructing a robust antitumor response to tumor cells create strategies for therapeutic success[5]. Currently, a novel strategy has been developed that causes a kind of apoptosis known as immunogenic cell death (ICD), a process that can inform the immune system of the existence of dying cancer cells[6−10]. ICD releases or expresses a set of dead cell-derived antigens, including adenosine triphosphate (ATP), calreticulin (CRT), heat-shock proteins (HSPs), high mobility group box 1 (HMGB1), ANXA1[11−13], and binding of these danger-associated molecular patterns (DAMPs) eventually results in a T cell-mediated immune response and uniquely killing cancer cells[14−16]. The stimulation of ICD is regarded as stressor-dependent induced by endoplasmic reticulum (ER) stress or reactive oxygen species (ROS)[17,18]. Based on these views, the majority of ICD inducers are identified and divided into two groups: type I and type II ICD inducers. Chemotherapeutic drugs, such as anthracyclines (idarubicin and doxorubicin)[19], cardiac glycosides (digoxin and ouabain)[20], and oxaliplatin[21], which target subcellular components such as plasma membrane proteins, cytosolic proteins, or DNA, resulting in indirect ER stress-induced apoptosis, belong to type I ICD inducers[22,23]. The physical modality of type II ICD inducers has been rarely reported. Photodynamic therapy (PDT) has been confirmed to produce ROS within cancer cells and most probably cause the dysfunction of ER directly[24−29]. Of note, physical ICD inducers show more advantages than chemotherapeutic drugs, owing to the severe side effects of chemotherapy added to patient suffering. Thus, the creation of *de novo* physical ICD inducers to expand the type II method will be an urgent, but outstanding strategy for effective cancer treatment.

Here, we focused on developing an alternative physical type II ICD inducer from enzyme-instructed and mitochondria-targeting peptide self-assembly. Our starting point is based on the mechanism of the "ROS-induced ROS release (RIRR)" phenomenon[30], where oxidative stress induced by external stimuli causes the collapse of the mitochondrial membrane potential, resulting in the release of more ROS and injury to neighboring mitochondria in a positive feedback loop[31]. Of the available approaches producing cell stresses, the self-assembly peptides have shown unique properties for generating endogenous or exogenous stresses toward cancer cells without affecting normal tissues[32−37]. Therefore, we combined these strategies to design a mitochondria-targeting self-assembling peptide (F-pY-T) as an ICD inducer by integrating triphenylphosphonium (TPP)[38−41] with the peptide (F-pY), as shown in Fig. 1A. In addition, liver accumulation is a limitation for directly delivering nanosized structures compared to monomers, which have poor retention time at the tumor site, although they show better penetration. Therefore, we employed the concept of enzyme-instructed self-assembly (EISA) in our design and conjugated flufenbuprofen (Fbp), an anti-inflammatory drug, as an aromatic capping group, with the phosphorylated D-tyrosine (p^DY)-containing pentapeptide to improve solubility, among which the sequence $G^DF^DF^DY$ has been proven to stimulate immune responses as an immune adjuvant[42]. Phosphorylated D-tyrosine (p^DY) is the substrate of alkaline phosphatase (ALP) overexpressed in cancer cells[43,44]. Therefore, we hypothesized that monomers of the peptide F-pY-T accumulate in the tumor site and that the dephosphorylation of phosphorylated D-tyrosine by ALP triggers self-assembly and forces the formation of nanostructures. These nanostructures have to face the fate of lockdown within lysosomes similar to other nanomaterials after internalization into cancer cells; therefore, the TPP-modified lysine residue head plays an important role in the proton sponge effect to help escape from lysosomes. Finally, F-Y-T nanostructures target mitochondria, cause oxidative stress, and induce immunogenic cell death *in vitro* and *in vivo*.

2. Materials and methods

2.1. Materials

2-Chlorotrityl chloride resin (1.2 mmol/g) was purchased from Nankai University resin Co., Ltd. Fmoc-amino acids were obtained from GL Biochem (Shanghai, China). Cy5.5 NHS ester (non-sulfonated) purchased from APEXBIO. Alkali phosphatase (30 U/μL) was obtained from Takara (D2250, Dalian, China) Bio. Inc. Enhanced ATP Assay Kit (S0027) purchased from Beyotime. Both of anti-HMGB1 antibody (ab79823) and anti-carlreticulin antibody (ab92516) were purchased from Abcam. Calreticulin Rabbit mAb (Alexa Fluor 488 conjugate, #62304) was obtained from Cell Signaling Technology. HMGB1 ELISA Kit (OKEH00424) was purchased from AVIVA systems biology. InvivoMAb antimouse PD-L1 (B7-H1) was obtained from Bio-Xcell. APC anti-mouse CD3 antibody (100235), FITC anti-mouse CD8a antibody (100705), APC anti-mouse IFN-γ (505810), PE anti-mouse CD80 (104707), FITC anti-mouse CD86 (105005), Alexa Fluor 647 anti-mouse CD11c (117314), ELISA MAX™ Deluxe Mouse IFN-γ, ELISA MAX™ Deluxe Mouse TNF-α and ELISA MAX™ Deluxe Mouse IL-6 were purchased from Biolegend. Collagenase IV and DNase I were both purchased from Solarbio. Commercially available reagents and solvents were used without further purification, unless noted otherwise.

2.2. TPP-modified peptide derivatives synthesis

We prepared the peptide derivatives by solid phase peptide synthesis (SPPS). 2-Chlorotrityl chloride resin and the corresponding *N*-Fmoc protected amino acids with side chains properly protected by a *tert*-butyl group (*t*Bu) or di-*tert*-butyl pyrocarbonate (Boc) was used in SPPS. HBTU was used as the coupling reagent. We used 95% of trifluoroacetic acid with 2.5% of TIS and 2.5% of H_2O to cleave peptide derivatives from resin and protection group from side chain for 60 min. The crude product (F-pY or F-Y) directly reacted with TPP-NHS, then reaction solution was purified by high performance liquid chromatography (HPLC) and then lyophilized to obtain pure products.

2.3. EISA convertion ratio of F-pY-T

The concentration of the work solution was 600 μmol/L. Na_2CO_3 (1 mol/L) was added to the above solution to adjust the final pH to 7.4. The solution was incubated at 37 °C for 5 min before adding alkali phosphatase (ALP, 0.1 U/mL) to the solution. 50 μL sample solution was added into 150 μL methanol solvent and then detected by LC–MS at different time point.

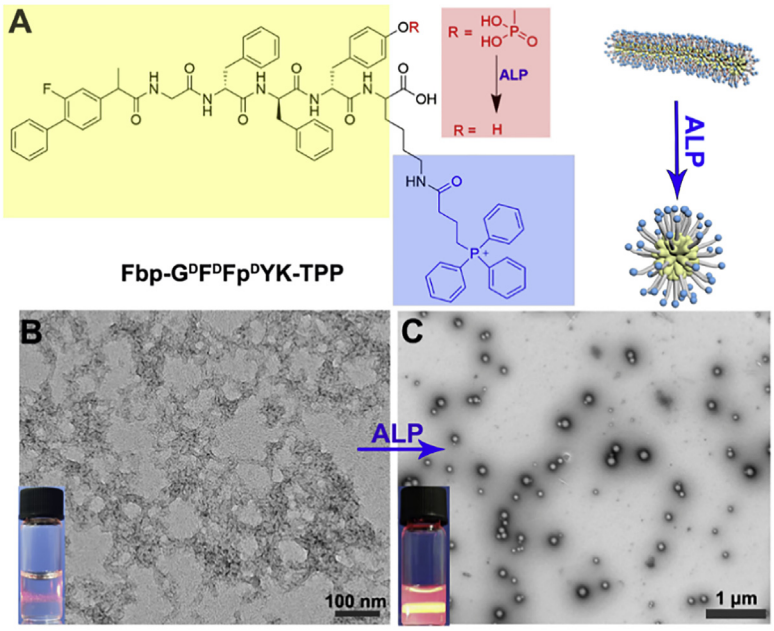

Figure 1 (A) Chemical structure of EISA mitochondria-targeting peptide conjugates F-pY-T; (B) TEM image of F-pY-T in solution (600 μmol/L) without adding ALP; (C) TEM image of F-pY-T (600 μmol/L) with ALP (0.1 U/mL) after 6 h incubation.

2.4. *Bio-TEM*

1×10^6 of CT26 cells were seeded in culture dish. After adherence, the cells were incubated with F-pY-T (600 μmol/L) for 6 h. Then, the medium was removed the cells were washed with cold PBS. Cell scraper was used to collect the cells and the medium containing cells was centrifuged at 1000 rpm for 3 min. The cells were rapidly placed into 2.5% glutaraldehyde overnight. Finally, the samples were observed under TEM by standard procedure.

2.5. *ROS detection*

1×10^5 of CT26 cells were seeded in CLSM culture dish. After adherence and removing the medium, cells were incubated with different compound solution including F-pY-T, F-Y-T, F-pY, and F-Y at concentration of 600 μmol/L for 24 h. Then the medium were removed the cells were washed with PBS for three times. After incubating with H2DCFDA for 30 min at 37 °C in the dark, the cells were washed with PBS three times. The fluorescence of FDA (oxidation of H2DCFDA) was detected by CLSM (λ_{exc} = 488 nm, λ_{em} = 510−570 nm).

2.6. *Apoptosis detection*

1×10^5 CT26 cells were seeded in 12-well culture dish. After adherence and removing the medium, cells were incubated with different compound solution including F-pY-T, F-Y-T, F-pY, and F-Y at concentration of 600 μmol/L for 24 h.Then, the medium was removed and the dish was washed with cold PBS for three times. The cells were trypsinized, centrifuged, resuspended in culture medium and stabilized in the cell incubator for 0.5 h. Finally, examination was performed under the manufacturer's instructions.

2.7. *Detection of ecto-CRT expression*

1×10^5 CT26 cells were seeded in CLSM culture dish. After adherence, cells were incubated with different compound including F-pY-T (600 μmol/L), F-Y-T (600 μmol/L), F-pY (600 μmol/L), F-Y (600 μmol/L), oxaliplatin (10 μmol/L) and control group for 24 h. Then, the medium was removed and the dish was washed with cold PBS for three times. For CLSM detection, the cells were first fixed with 4% paraformaldehyde for 15 min, then washed with PBS for three times and blocked with 10% goat serum PBST solution for 1 h. The fixed cells were incubated with anti-calreticulin antibody (1:500, 1% BSA PBST solution) overnight at 4 °C. After washed with PBST for three times, the cells were further incubated with Alexa Fluor 633 conjugated goat secondary antibody to Rabbit IgG (1:500) at room temperature for 1 h. Nuclear DNA was labelled in blue with DAPI. CLSM was used to check the expression of *ecto*-CRT. (DAPI: λ_{ex} = 405 nm, λ_{em} = 430−490 nm *ecto*-CRT: λ_{ex} = 633 nm, λ_{em} = 650−750 nm).

For flow cytometer, 2×10^5 CT26 cells were seeded in 6-well culture dish and incubated with different compound for 24 h at concentration of 600 μmol/L. After removing the medium and washing dish with cold PBS for three times. The cells were trypsinized and centrifuged. The cells were then incubated with Calreticulin Rabbit mAb (Alexa Fluor 488 conjugate, #62304, 1:200, 1% BSA PBS solution) at 4 °C for 30 min and washed with PBS for three times. Flow cytometer was used to test the *ecto*-CRT expression.

2.8. *Detection of ATP secretion and ecto-HMGB1*

The CT26 cells were seeded into 12-well plate at the density of 1×10^5 cells and incubated with F-pY-T (600 μmol/L), F-Y-T (600 μmol/L), F-pY (600 μmol/L), F-Y (600 μmol/L), oxaliplatin (10 μmol/L) and control group for 36 h, respectively. Next, the cell medium was collected and conducted with centrifugation (1200 rpm for 5 min at 4 °C). Then, the collected supernatants were centrifuged (12,000 rpm for 10 min at 4 °C). Finally, the ATP levels were immediately determined by ATP Bioluminescent assay kit according to manufacturer's instruction. The extracellular HMGB1 was analyzed by ELISA assay kit according to manufacturer's instruction.

2.9. Living animal image

All animal procedures were approved by the Centre of Tianjin Animal Experiment Ethics Committee. The accreditation number of the laboratory is SYXK (Jin) 2019−0003 promulgated by Tianjin Science and Technology Commission.

Each BALB/c mouse was subcutaneously injected with 2×10^6 CT26 cells on the right flank. When the tumor volume reached 200 mm^3, the mice were then intravenously injected with 200 μL of Cy5.5-pY-T at an identical Cyanine 5.5 dose of 0.1 mg per mouse ($n = 3$). Fluorescence imaging was performed using a IVIS Lumina II imaging (PerkinElmer, USA) at different time point postinjection. Mice were sacrificed after 72 h post-injection for fluorescence imaging of the major organs (*i.e.*, heart, liver, spleen, lung and kidney) and tumors *ex-vivo*.

2.10. ICD induction in vivo

BALB/c mice were injected with 1×10^6 CT26 cells on the right flank (sc). When tumor volume reached to ~70 mm^3, the mice were randomly divided into 3 groups. Then the mouse was treated with PBS, 10 and 30 mg/kg F-pY-T *via* tail intravenous injection for three times every three days. On Day 8, the mice were sacrificed and tumor tissues were collected to detect the levels of *ecto*-CRT *via* standard tissue immunofluorescence staining.

2.11. Tumor treatment

When CT26 tumor volume reached to ~70 mm^3, the mice were randomly divided into 4 groups ($n = 8$) and accepted the treatment. The tumor volume and body weight was monitored for every 2 days and the tumor volume calculated by Eq. (1):

$$V = L \times W \times W/2 \quad (1)$$

where L represents the longest dimension, W represents the shortest dimension.

2.12. DC maturation

CT26-tumor bearing BALB/c mice were treated with various formulations. The inguinal lymph nodes (LNs) were harvested on Day 9. The ratio of DC maturation in the LNs was then examined by flow cytometry after immunofluorescence staining with anti-CD11c-AF647, anti-CD80-PE and anti-CD86-FITC antibodies. Meanwhile, blood biochemistry and blood hematology was also carried out. Five major organs (heart, liver, spleen, lung, and kidney) were harvested to detect the tissue damage by H&E staining.

2.13. T lymphocytes infiltration

Mice bearing CT26 tumors (approximately 70 mm^3) were injected with PBS (iv), anti-PD-L1 (ip), F-pY-T (iv) and F-pY-T (iv) plus anti-PD-L1 (ip) every 3 days for 3 times, respectively. After treatment and monitoring (15th day), the mouse was sacrificed and the tumor tissue was harvested. The harvested tumors were cut into small pieces and immersed in the solution of 1.0 mg/mL collagenase IV and 0.4 mg/mL DNase I for 60 min at 37 °C to obtain a single cell suspension. $CD8^+$ T cells were stained with anti-CD3-APC, anti-CD8a-FITC antibody. IFN-γ^+CD8^+ T lymphocytes were stained with anti-CD8a-FITC and anti- IFN-γ-APC antibodies before flow cytometry.

2.14. Cytokine secretion

The mice bearing CT26 tumor (about 100 mm^3) were injected with PBS (iv), anti-PD-L1 (ip), F-pY-T (iv) and F-pY-T (iv) plus anti-PD-L1 (ip) at first day, separately. Then, the mice were sacrificed to harvest the tumor tissue on Days 1 (before injection), 3 and 7, respectively. The tumor tissue was weighed, cut into pieces and homogenized, added with protease inhibitors and DNase I and ultrasonically broken. Finally, IFN-γ, IL-6 and TNF-α were measured by ELISA kit according to the manufacturer's instructions.

2.15. Statistical analysis

Data were analysed by Prism 8 (GraphPad Software). Multiple comparisons were described in the figure captions.

3. Results and discussions

3.1. Design and synthesis of peptide molecules

Our designed peptide, Fbp-$G^DF^DFp^DYK$-TPP (F-pY-T, Fig. 1A), underwent a simple and straightforward synthetic process (Supporting Information Fig. S1). First, the Fbp-$G^DF^DFp^DYK$ sequence was synthesized through standard solid phase peptide synthesis. The *N*-hydroxysuccinimide (NHS)-activated TPP derivative was coupled with the ε-amino group of the lysine residue, resulting in the target compound. We also obtained control compounds *via* a similar route, including Fbp-$G^DF^DF^DYK$-TPP (F-Y-T, without phosphorylation), Fbp-$G^DF^DFp^DYK$ (F-pY, without TPP moiety), and Fbp-$G^DF^DF^DY$ (F-Y). All the compounds were purified using high performance liquid chromatography (HPLC) and identified using high resolution mass spectrometry (HR-MS, Supporting Information Figs. S2–S5).

3.2. Enzyme instructed self-assembly

Direct dissolution of F-pY-T in phosphate-buffered saline (PBS, pH = 7.4) at a concentration of 600 μmol/L yielded a clear solution compared to the unphosphorylated F-Y-T, which was slightly soluble in PBS under the same conditions (Supporting Information Fig. S6). Transmission electron microscopy (TEM) images revealed the existence of nanofibril-like structures with a diameter of 15−20 nm in F-pY-T solution (600 μmol/L, Fig. 1B). After adding ALP (0.1 U/mL) into the F-pY-T solution and incubating at 37 °C for 6 h, the solution turned opalescent, and nanoparticles roughly 100−150 nm in diameter, instead of nanofibrils, were observed under TEM (Fig. 1C and Supporting Information Fig. S7). The Zeta potential of F-pY-T solution, as shown in Supporting Information Fig. S8, was also changed from electronegativity to neutrality due to the enzymatic dephosphorylation. The LC–MS trace further demonstrated that over 93% of F-pY-T was converted to F-Y-T after incubation with ALP within 12 h (Supporting Information Fig. S10).

3.3. Mitochondrial targeting peptides regulate CT26 cell fate

To investigate the cellular response and oxidative stress induced by the test compounds, intracellular ROS levels of mouse colon carcinoma CT26 cells cultured with different compounds (F-Y, F-pY, F-Y-T, and F-pY-T) were detected using 2′,7′-

dichlorodihydrofluorescein diacetate (H2DCFDA) as an indicator and untreated CT26 cells were used as a control. As shown in Fig. 2B, bright green fluorescence was observed in the CT26 cells treated with F-pY-T for 24 h through confocal laser scanning microscopy (CLSM), in stark contrast to the extremely weak green fluorescence appearing in other groups. The semi-quantitative analysis of fluorescence intensity from CLSM images (Fig. 2D) also demonstrated the strong ability of F-pY-T to promote ROS production compared to the other three compounds. The introduction of the TPP moiety into the peptide sequence was an essential prerequisite for the observed ROS production when comparing F-pY-T and F-Y-T with F-Y and F-pY. Bio-TEM image indeed provides a critical explanation for the remarkable ROS production following F-pY-T treatment, as shown in Supporting Information Figs. S11 and S12. Compared to the untreated CT26 cells, F-pY-T nanoparticles were visible within the mitochondria of the cells after treatment, along with a significant change in mitochondrial morphology, which was thought to produce serious oxidative stress. Additionally, we thought that F-Y-T showing much weaker ability to induce ROS than F-pY-T might originate from the structure size of pre-synthesized F-Y-T, which is much larger and more difficult to internalize by the cells than that of the slow self-assembly of enzymatically hydrolyzed production of F-Y-T from F-pY-T. Flow cytometry was used to determine the apoptotic status of the cells after ROS production was confirmed. As shown in Fig. 2C and E, approximately 65.1% of the CT26 cells treated with F-pY-T were in the early apoptotic state (Annexin^{+}/PI^{-}), while the majority of cells treated with other compounds remained normal, indicating that F-pY-T might be able to trigger the ICD procedure.

3.4. *The ability evaluation of ICD induced by different compound in vitro*

To further examine the ability of F-pY-T to induce immunogenic cell death, DAMPs, including *ecto*-CRT, HMGB1 release (*ecto*-HMGB1), and ATP secretion were evaluated in the CT26 cell lines treated with our synthetic compounds. Oxaliplatin was used as a positive control *in vitro*. As an "eat me" signal[45], calreticulin (CRT) exposure at the cell surface (*ecto*-CRT) is the gold standard for judging ICD induction. The levels of *ecto*-CRT in CT26 cells treated with different compounds were determined using immunofluorescence (IF) staining. After incubation of the CT26 cells with the test compounds for 24 h, the standard IF staining procedures for CLSM detection were performed[45]. As shown in Fig. 3A and Supporting Information Fig. S13, characteristic red-colored surface patches from the Alexa Fluor 633-conjugated secondary antibody were visualized in the F-pY-T group, indicating the translocation of CRT from its orthotopic localization within the lumen of ER vesicles to the surface of tumor cells. Consistent with the comparison of ROS production, F-Y-T could also induce *ecto*-CRT against the CT26 cells, but the fluorescence intensity was much weaker. In the other groups, *ecto*-CRT was barely exhibited, even with oxaliplatin. The semi-quantitative analysis of fluorescence intensity from CLSM images (Supporting Information

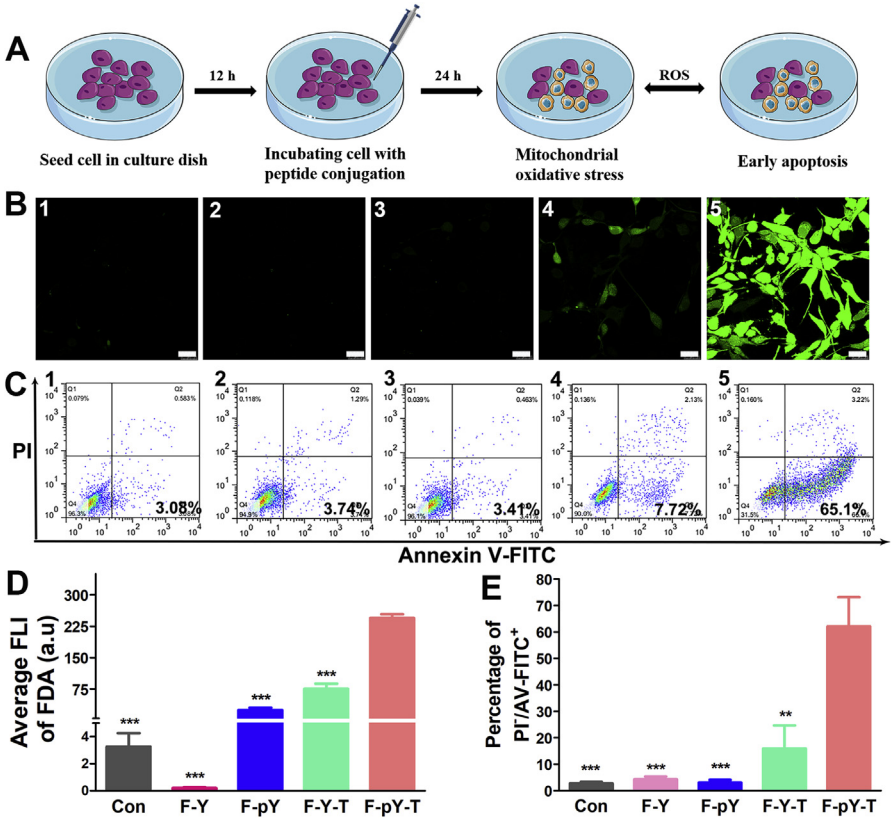

Figure 2 (A) Scheme of the detection assay for ROS and apoptosis; (B) CLSM images of the CT26 cells treated with different compounds (1: Control, 2: F-Y, 3: F-pY, 4: F-Y-T, and 5: F-pY-T) after monitoring ROS production levels using H2DCFDA as an indicator. Scale bars represent 25 μm; (C) Representative flow cytometry plots indicate the proportions of early apoptosis in the CT26 cells (1: Control, 2: F-Y, 3: F-pY, 4: F-Y-T, and 5: F-pY-T); (D) Semi-quantitative analysis of average FDA fluorescence intensity; (E) Percentage of early apoptosis (PI^{-}/Annexin V^{+}) in different groups. One-way ANOVA, mean ± SD, ***$P < 0.001$, **$P < 0.01$. $n = 3$.

Fig. S14) and flow cytometry (Fig. 3B) also confirmed this observation. In addition, the induction of *ecto*-CRT by F-pY-T was dose-dependent at concentrations below 300 μmol/L (Supporting Information Fig. S15) and an obvious time-dependent increase was observed from 12 to 18 or 24 h (Supporting Information Fig. S16).

In addition to checking the exposure of CRT on the cell surface, two other typical hallmarks, the secretion of adenosine triphosphate (ATP) and the release of high mobility group B1 (HMGB1), were also monitored. As shown in Fig. 3C, the ATP concentration in the supernatant of the different treatment groups was measured, and we found that F-pY-T significantly induced a higher secretion of ATP than the other groups. The release of HMGB1 was determined by enzyme-linked immunosorbent assay (ELISA) and IF staining. In Fig. 3E, we found out that HMGB1 was predominantly located in the nucleus of the untreated CT26 cells while it was almost completely released from the nucleus in the F-pY-T group, which was in accordance with the ELISA results that F-pY-T promoted the most release of HMGB1 than the other compounds (Fig. 3D). Together, these data strongly demonstrate that EISA-induced mitochondrial oxidative stress is a promising modality to evoke massive ICD (Fig. 3F).

3.5. *Evaluation of accumulation and retention of EISA mitochondrial targeting peptide in tumor sites*

Next, the accumulation and retention at the tumor site of our designed concept were investigated by changing the Fbp group to cyanine-5.5, enabling the new synthetic model molecule (Cy5.5-pY-T, Supporting Information Figs. S17 and S18) to be visualized through *in vivo* imaging systems. We employed CT26 tumor-bearing BALB/c mice to evaluate their accumulation and retention capacity in solid tumors after intravenous injection of Cy5.5-pY-T (0.1 mg Cy5.5-equivalent dose per mouse, $n = 3$). As shown in Fig. 4A and B, Cy5.5-pY-T was enriched at the tumor site at 4 h after administration, and the quantitative fluorescence statistics showed that the fluorescence intensity reached a maximum at this time point. The observation time was extended to investigate the retention capacity of Cy5.5-pY-T. There was no significant decrease in fluorescence intensity at the tumor site from 12 to 72 h, which indicated that Cy5.5-pY-T had excellent accumulation and a long retention capacity. The main organs and tumor tissues were harvested 72 h after administration to further investigate the biodistribution of Cy5.5-pY-T in the body of the mouse *ex vivo*. The fluorescence intensity of the tumor tissue was higher than that of the other organs (Supporting Information Fig. S19), which was consistent with the *in vivo* results. In addition, *ex vivo* images exhibited a strong fluorescence intensity in the kidney, indicating that Cy5.5-pY-T was mainly removed by renal clearance. Together, these results showed that the EISA mitochondria-targeting compound was capable of effectively accumulating and retaining in tumor tissue, which was essential for inducing large-scale ICD.

3.6. *The evaluation of ICD inducing by F-pY-T in vivo*

Having demonstrated the ICD induction property *in vitro* and the accumulation and retention capacity of our design, we further

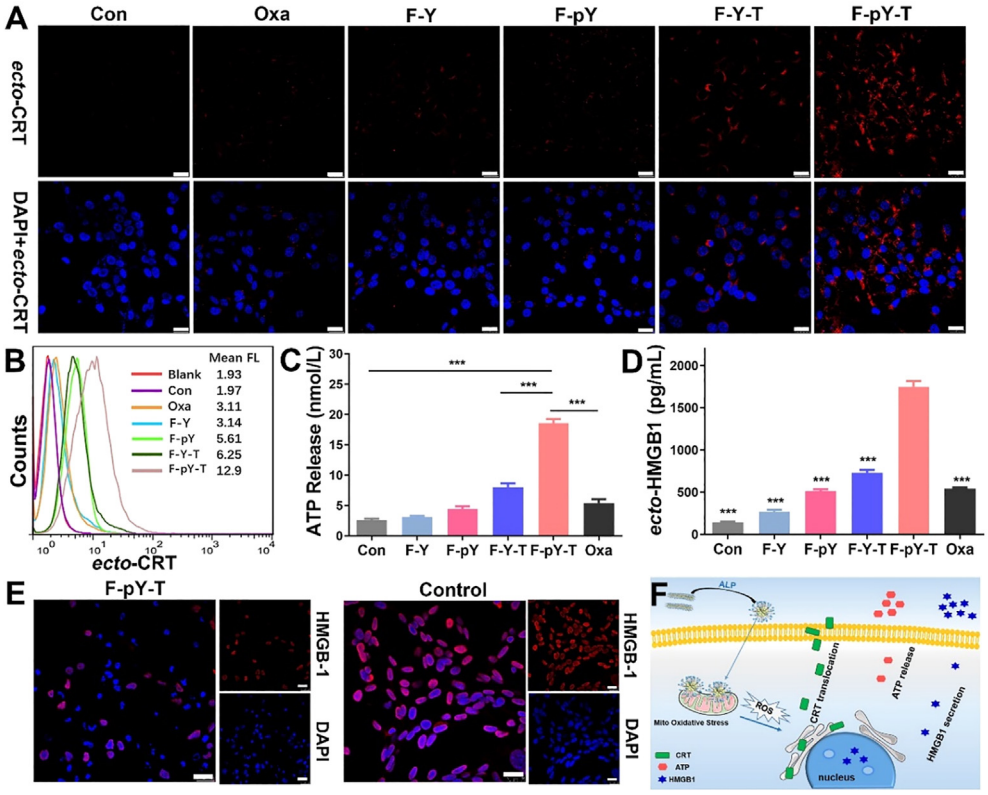

Figure 3 (A) CLSM images of *ecto*-CRT levels on CT26 cells treated with different compounds for 24 h. The cell nucleus was stained with 4′,6-diamidino-2-phenylindole (DAPI: blue fluorescence). The scale bars represent 25 μm; (B) Flow cytometric analysis of ICD induction in CT26 cells *in vitro* with or without treatment with different compounds; Quantitative analyses of (C) ATP and (D) HMGB1 in the cell supernatants. One-way ANOVA, mean ± SD, $^{***}P < 0.001$, $^{**}P < 0.01$. $n = 3$; (E) Immunofluorescence CLSM images of CT26 cells treated with or without F-pY-T. The scale bar represents 25 μm; (F) Schematic illustration of the ICD induction profile of F-pY-T.

investigated the induction of ICD *in vivo* and the antitumor efficacy of F-pY-T in a BALB/c mouse model bearing CT26 tumors. First, we chose three dosage groups of F-pY-T for ICD induction, including 0 (control), 10, and 30 mg/kg, and the mice were treated with F-pY-T *via* the tail vein every 3 days for three times totally. The mice were sacrificed on Day 8 to harvest the tumor tissues. The tumor tissues were then frozen, sectioned, and subjected to standard IF staining to observe *ecto*-CRT expression *via* CLSM. As shown in Fig. 4C and Supporting Information Fig. S20, there was almost no *ecto*-CRT exposure in the control group, but a dramatically high expression was observed in the 10 or 30 mg/kg dosage groups, indicating that F-pY-T could induce ICD *in vivo*.

3.7. *The anti-tumor efficacy assessment*

We then checked the antitumor efficacy of F-pY-T in a tumor-bearing BALB/c mouse model, accompanied with a combination of immune checkpoint blockade (ICB) therapy using anti-PD-L1 agents. When the tumor volume reached approximately 70 mm^3, the mice were randomly divided into four groups and treated with different drugs, including F-pY-T plus anti-PD-L1 (10 mg/kg F-pY-T iv for 24 h, then 75 μg anti-PD-L1 per mouse ip once every three days, $n = 8$), F-pY-T (10 mg/kg iv), anti-PD-L1 (75 μg anti-PD-L1 per mouse ip), and PBS (control), as illustrated in Fig. 4D. Compared with the control, anti-PD-L1 agents suppressed the tumor to an extent, but the effect varied among individuals. Impressively, F-pY-T exhibited a decent antitumor efficacy, and this dramatic effect was further elevated with the combination of F-pY-T and an anti-PD-L1 agent (Fig. 4E). Finally, the tumor weight and volume were evaluated, and the results showed that combination therapy significantly inhibited tumor growth (Fig. 4F and G). All these findings demonstrated that F-pY-T-mediated ICD not only suppressed tumor growth, but also effectively boosted the therapeutic efficacy of ICB.

3.8. *The mechanism analysis of anti-tumor immunity*

To ascertain the mechanism of antitumor immunity using F-pY-T and combination therapy, we investigated the performance of the F-pY-T activated immune response *in vivo*. Antigen-presenting

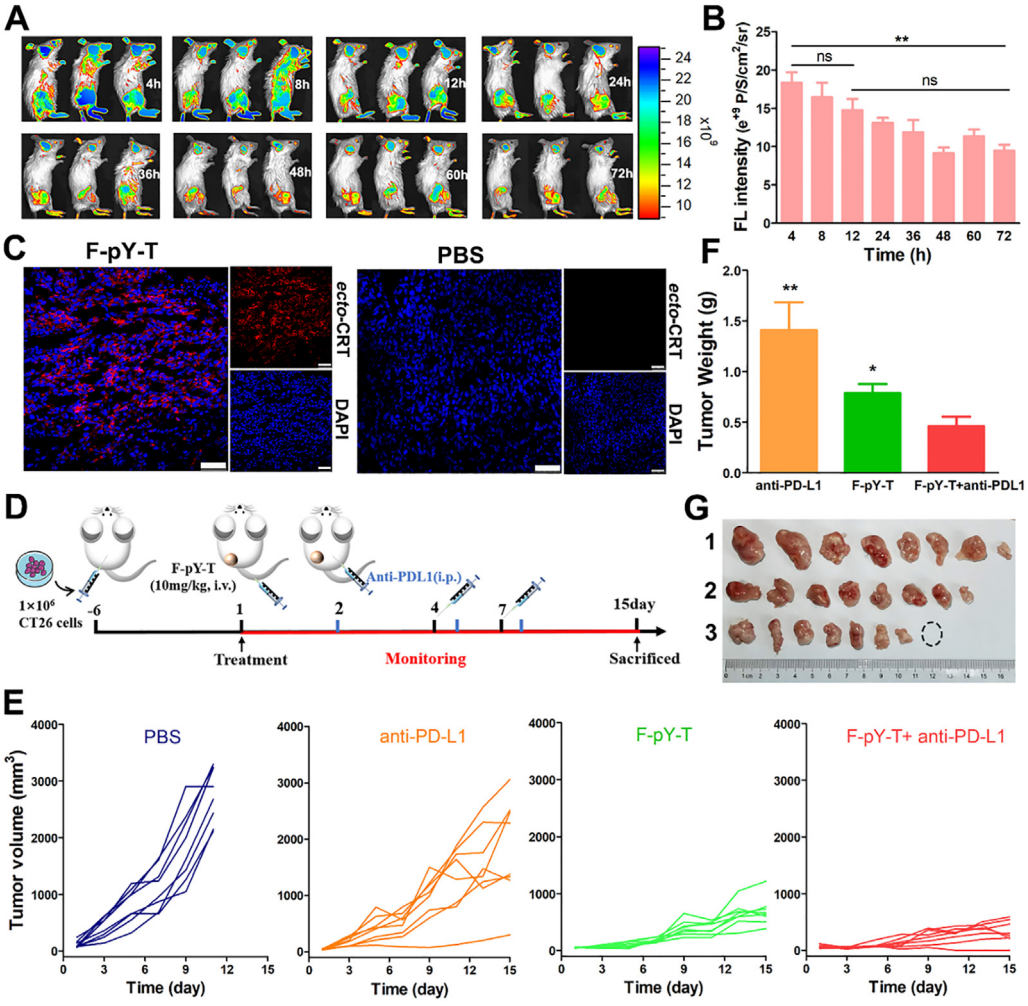

Figure 4 (A) NIR fluorescence imaging of the biodistribution of Cy5.5-labeled peptide conjugates in CT26 tumor-bearing BALB/c mice *in vivo*; (B) Quantitative fluorescence analyses of (A) at the corresponding time; (C) Immunofluorescence CLSM images of CRT induction by F-pY-T in the CT26 tumor-bearing BALB/c mice *in vivo*. The scale bars represent 50 μm; (D) Schematic illustration of F-pY-T and anti-PD-L1 blockade-mediated combination therapy; (E) Single-component tumor growth curves ($n = 8$); (F) Tumor weight in the different groups. Two-tailed *t*-test, $^{***}P < 0.001$, $^{**}P < 0.01$, $^{*}P < 0.05$. $n = 8$; (G) Optical image of tumors (1: anti-PD-L1, 2: F-pY-T, and 3: F-pY-T plus anti-PD-L1).

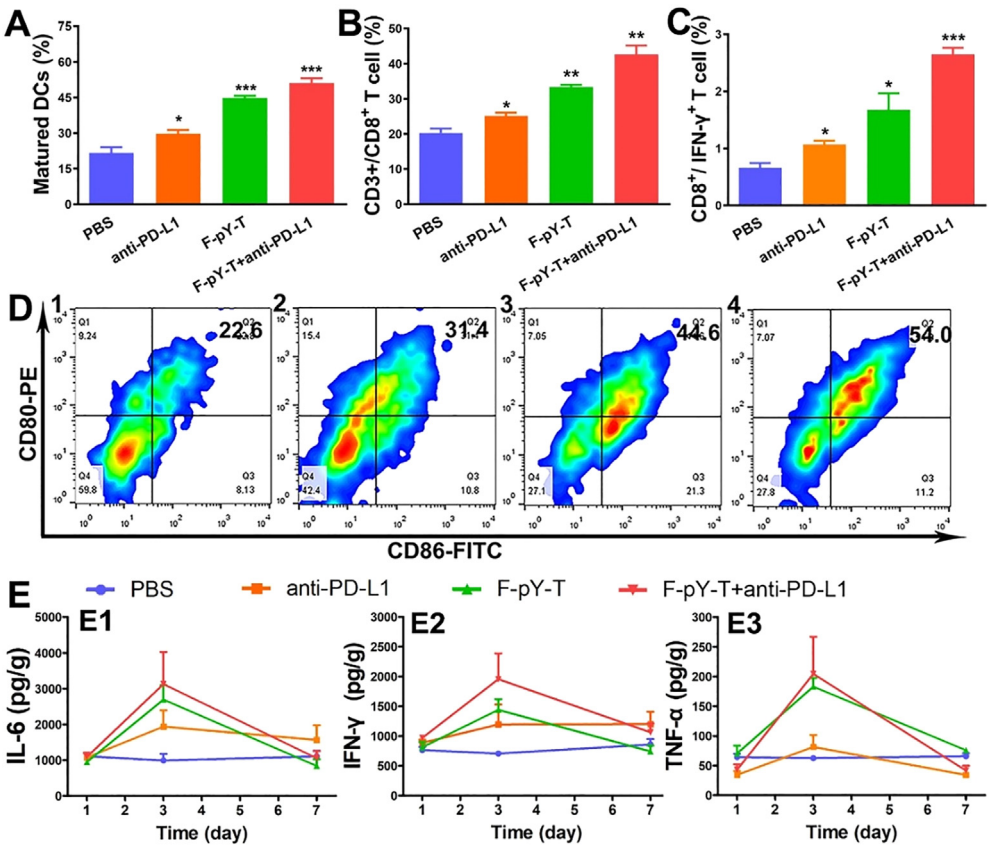

Figure 5 Flow cytometric examination of (A) DC maturation rates in the LNs (gated on $CD11c^+$), (B) intratumoral infiltration of $CD8^+$ (gated on $CD3^+$), and (C) IFN-γ^+CD8^+ T lymphocytes in total tumor tissue on Days 9 and 15, respectively. Two-tailed *t*-test, mean ± SD, $^{***}P < 0.001$, $^{**}P < 0.01$, $^{*}P < 0.05$, $n = 3$, PBS group as control. (D) Representative flow cytometry plots indicate the matured DCs (LNs) of 1) PBS, 2) anti-PD-L1, 3) F-pY-T, 4) F-pY-T + anti-PD-L1 *in vivo*. (E) ELISA analysis of secretion of IL-6, IFN-γ, and TNF-α in tumor tissues with various treatments ($n = 3$).

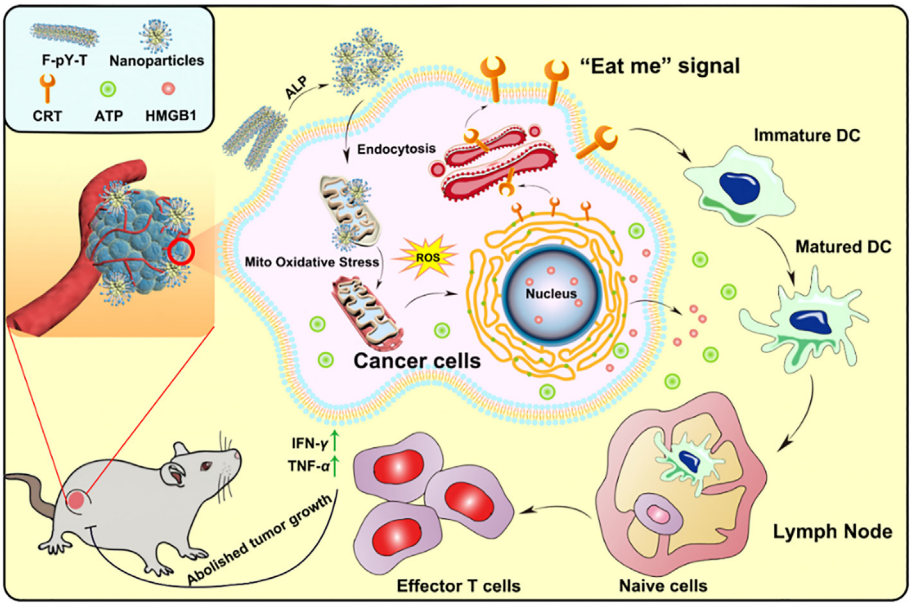

Figure 6 Schematic mechanism of F-pY-T-mediated ICD to abolish tumor growth.

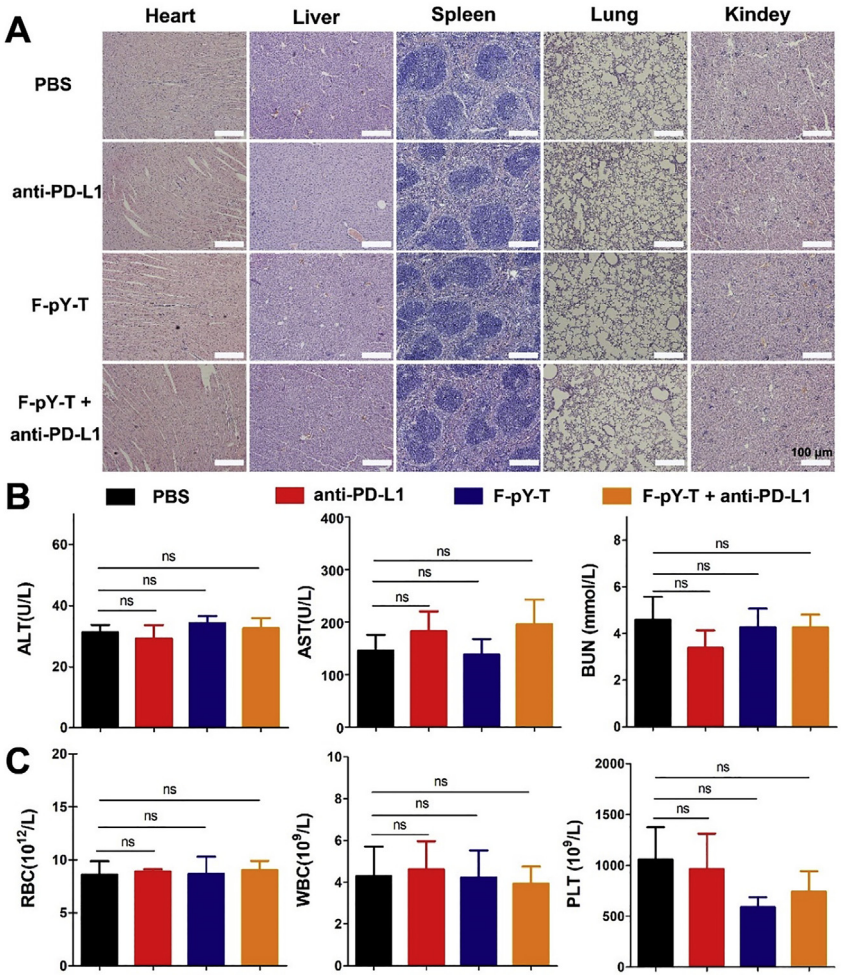

Figure 7 (A) Five major organs haematoxylin and eosin (H&E) staining images after treatment, scale bar represents 100 μm. Important index values of (B) blood biochemistry test and (C) blood hematology test. Two-tailed student's *t*-test, compared with PBS group, mean ± SD, $n = 3$, ns represents no significant.

cells, particularly dendritic cells (DCs), play a vital role in activating and regulating the immune system[46]. Moreover, mature DCs present antigens to cytotoxic T lymphocytes (CTLs), resulting in the reestablishment of immune surveillance and induction of immune-mediated killing[47]. Therefore, we evaluated DC maturation in the tumor-draining lymph nodes (LNs) using flow cytometry and intratumoral infiltration of CTLs ($CD3^+$/$CD8^+$) on Days 9 and 15, respectively. DC maturation ($CD11c^+$/$CD80^+$/$CD86^+$) percentage in the anti-PD-L1 and PBS groups was approximately 29.7% and 21.6%, respectively, while that of the F-pY-T group and F-pY-T plus anti-PD-L1 group was dramatically increased to approximately 44.7% and 50.1%, respectively (Fig. 5A and D), indicating that DAMPs from F-pY-T-induced ICD could stimulate the maturation of DCs. Additionally, as shown in Fig. 5B and Supporting Information Fig. S21, the intratumoral infiltrating CTLs F-pY-T plus anti-PD-L1, F-pY-T, anti-PD-L1, and the control groups were approximately 42.63%, 33.3%, 25.1%, and 20.3%, respectively. Furthermore, the ratio of interferon-γ^+ (IFN-γ^+) effector $CD8^+$ T cells in total tumor tissue was measured using flow cytometry, and the results were shown in Fig. 5C and Supporting Information Fig. S22. Here it was demonstrated that the combination therapy could substantially enhance the ratio of IFN-γ^+ effector $CD8^+$ T cells, which was 1.59-, 2.49-, and 3.99-fold higher than that of F-pY-T, anti-PD-L1, and control groups, respectively. Collectively, these findings indicated that the combination therapy had the highest effectiveness in reestablishing immune responses by promoting the maturation of DCs and activating CTLs *in vivo*.

Another representative hallmark of tumor cell apoptosis during immune responses is the secretion of pro-inflammatory cytokines[48]. Therefore, the tumor tissues were harvested at different time points and the relevant levels of interleukin-6 (IL-6), interferon-γ (IFN-γ), and tumor necrosis factor-α (TNF-α) were analyzed using an ELISA kit after the first administration in the CT26 tumor-bearing mice. As shown in Fig. 5E, compared to Day 1, the secretion levels of all three intratumoral cytokines increased to a certain extent in the anti-PD-L1, F-pY-T, and F-pY-T plus anti-PD-L1 groups on Day 3 (post-administration for two days). In terms of IL-6, the value of the F-pY-T plus anti-PD-L1 group was significantly higher than that of the other three groups (1.16-, 1.61-, and 3.15-fold for F-pY-T, anti-PD-L1, and control groups, respectively). The IFN-γ levels in the F-pY-T plus anti-PD-L1 group were 1.36-, 1.64-, and 2.74-fold higher than those in the F-pY-T, anti-PD-L1, and control groups, respectively. For the secretion of TNF-α, the F-pY-T plus anti-PD-L1 group gave rise to a similar tendency, showing 1.12-, 2.5-, and 3.19-fold higher than that of the F-pY-T, anti-PD-L1,

and PBS groups, respectively. All these data confirm that F-pY-T-mediated ICD could result in a pro-inflammatory response. Moreover, the concentration of these pro-inflammatory cytokines gradually attenuated to basal levels on Day 7 (six days post-administration), which confirmed the acute immune inflammatory response caused by the treatment. Thus, it was reasonable to conclude that F-pY-T and combination therapy could trigger adaptive antitumor immunity *in vivo* (Fig. 6).

3.9. The biosafety evaluation of all three therapeutic formulations

Finally, the *in vivo* toxicity of all three therapeutic formulations was evaluated (anti-PD-L1, F-pY-T, and F-pY-T plus anti-PD-L1). As shown in Supporting Information Fig. S23, the mice in all the groups did not show obvious bodyweight reduction during the entire treatment period. Tissues from the heart, liver, spleen, lung, and kidney in all the groups were analyzed using hematoxylin and eosin (H&E) staining, and no obvious cell damage or histopathological changes were observed compared to the control group (Fig. 7A). The results of serum biochemistry and blood hematology assays also indicated that the main detection values were all within the reference range (Fig. 7B and C, and Supporting Information Fig. S24), suggesting the good biosafety of our developed nanomedicines.

4. Conclusions

In this study, we successfully developed an alternative physical type II ICD inducer by adopting an EISA and a mitochondrial-targeting strategy, in which nanoparticles formed from the enzyme-responsive peptide F-pY-T showed a specific ability to induce focused mitochondrial oxidative stress in cancer cells. In accordance with other ICD inducers, F-pY-T is expected to induce the apoptosis of cancer cells, which, along with the release of DAMPs, promotes the maturation of DCs and activates CTLs *in vivo*. The reestablished antitumor immunity not only inhibits tumor growth but also enhances antitumor efficiency in immune checkpoint blockade (ICB) therapy by combining F-pY-T and anti-PD-L1. This study also reals the advantage of our concept without using any chemotherapeutic drugs as inducers, exhibiting specific bio-distribution and invisible toxicity *in vivo*. This strategy of evoking ICD through mitochondria-targeting oxidative stress induced by drug/photosensitizer-free design provides a new viewpoint for cancer immunotherapy.

Acknowledgments

This work was supported by the National Natural Science Foundation of China (31870949, 21875116, 31961143004, 81921004, 81100942, 81472081), the National Science Fund for Distinguished Young Scholars (31825012, China) and the Tianjin Science Fund for Distinguished Young Scholars (17JCJQJC44900, China). We also thank Dr. Wenjing Li and Dr. Zhiwen Hu for their help in this work.

Author contributions

Debin Zheng, Jingfei Liu, Yinghao Ding, and Rong Peng synthesized and characterized the compounds. Debin Zheng, Jingfei Liu and Limin Xie performed the cell and animal experiments. Debin Zheng, Yinghao Wang and Min Cui analysed the results and performed the scheme illustration. Ling Wang, Yongjie Zhang, Chunqiu Zhang, and Zhimou Yang guided the research, wrote the manuscripts and acquired Funding.

Conflicts of interest

The authors declare that they have no known competing financial interests or personal relationships that could have appeared to influence the work reported in this paper.

Appendix A. Supporting information

Supporting information to this article can be found online at https://doi.org/10.1016/j.apsb.2021.07.005.

References

1. Wolchok JD, Chiarion-Sileni V, Gonzalez R, Rutkowski P, Grob JJ, Cowey CL, et al. Overall survival with combined nivolumab and ipilimumab in advanced melanoma. *N Engl J Med* 2017;**377**:1345–56.
2. Smyth MJ, Ngiow SF, Ribas A, Teng MW. Combination cancer immunotherapies tailored to the tumour microenvironment. *Nat Rev Clin Oncol* 2016;**13**:143–58.
3. Zhang X, Wang C, Wang J, Hu Q, Langworthy B, Ye Y, et al. PD-1 blockade cellular vesicles for cancer immunotherapy. *Adv Mater* 2018;**30**:e1707112.
4. Seliger B, Massa C. Immune therapy resistance and immune escape of tumors. *Cancers (Basel)* 2021;**13**:551.
5. Tesniere A, Panaretakis T, Kepp O, Apetoh L, Ghiringhelli F, Zitvogel L, et al. Molecular characteristics of immunogenic cancer cell death. *Cell Death Differ* 2008;**15**:3–12.
6. Showalter A, Limaye A, Oyer JL, Igarashi R, Kittipatarin C, Copik AJ, et al. Cytokines in immunogenic cell death: applications for cancer immunotherapy. *Cytokine* 2017;**97**:123–32.
7. Galluzzi L, Buque A, Kepp O, Zitvogel L, Kroemer G. Immunogenic cell death in cancer and infectious disease. *Nat Rev Immunol* 2017;**17**:97–111.
8. Kroemer G, Galluzzi L, Kepp O, Zitvogel L. Immunogenic cell death in cancer therapy. *Annu Rev Immunol* 2013;**31**:51–72.
9. Bezu L, Gomes-de-Silva LC, Dewitte H, Breckpot K, Fucikova J, Spisek R, et al. Combinatorial strategies for the induction of immunogenic cell death. *Front Immunol* 2015;**6**:187.
10. Zhou J, Wang G, Chen Y, Wang H, Hua Y, Cai Z. Immunogenic cell death in cancer therapy: present and emerging inducers. *J Cell Mol Med* 2019;**23**:4854–65.
11. Clarke C, Smyth MJ. Calreticulin exposure increases cancer immunogenicity. *Nat Biotechnol* 2007;**25**:192–3.
12. Green DR, Ferguson T, Zitvogel L, Kroemer G. Immunogenic and tolerogenic cell death. *Nat Rev Immunol* 2009;**9**:353–63.
13. Krysko DV, Agostinis P, Krysko O, Garg AD, Bachert C, Lambrecht BN, et al. Emerging role of damage-associated molecular patterns derived from mitochondria in inflammation. *Trends Immunol* 2011;**32**:157–64.
14. Krysko DV, Garg AD, Kaczmarek A, Krysko O, Agostinis P, Vandenabeele P. Immunogenic cell death and DAMPs in cancer therapy. *Nat Rev Cancer* 2012;**12**:860–75.
15. Roh JS, Sohn DH. Damage-associated molecular patterns in inflammatory diseases. *Immune Netw* 2018;**18**:e27.
16. Schaefer L. Complexity of danger: the diverse nature of damage-associated molecular patterns. *J Biol Chem* 2014;**289**:35237–45.
17. Dudek AM, Garg AD, Krysko DV, De Ruysscher D, Agostinis P. Inducers of immunogenic cancer cell death. *Cytokine Growth Factor Rev* 2013;**24**:319–33.

18. Garg AD, Dudek-Peric AM, Romano E, Agostinis P. Immunogenic cell death. *Int J Dev Biol* 2015;**59**:131−40.
19. Casares N, Pequignot MO, Tesniere A, Ghiringhelli F, Roux S, Chaput N, et al. Caspase-dependent immunogenicity of doxorubicin-induced tumor cell death. *J Exp Med* 2005;**202**:1691−701.
20. Menger L, Vacchelli E, Adjemian S, Martins I, Ma Y, Shen S, et al. Cardiac glycosides exert anticancer effects by inducing immunogenic cell death. *Sci Transl Med* 2012;**4**:143ra99.
21. Tesniere A, Schlemmer F, Boige V, Kepp O, Martins I, Ghiringhelli F, et al. Immunogenic death of colon cancer cells treated with oxaliplatin. *Oncogene* 2010;**29**:482−91.
22. Zhang K, Kaufman RJ. Signaling the unfolded protein response from the endoplasmic reticulum. *J Biol Chem* 2004;**279**:25935−8.
23. Walter P, Ron D. The unfolded protein response: from stress pathway to homeostatic regulation. *Science* 2011;**334**:1081−6.
24. Garg AD, Krysko DV, Verfaillie T, Kaczmarek A, Ferreira GB, Marysael T, et al. A novel pathway combining calreticulin exposure and ATP secretion in immunogenic cancer cell death. *EMBO J* 2012;**31**:1062−79.
25. Garg AD, Vandenberk L, Koks C, Verschuere T, Boon L, Van Gool SW, et al. Dendritic cell vaccines based on immunogenic cell death elicit danger signals and T cell-driven rejection of high-grade glioma. *Sci Transl Med* 2016;**8**:328ra27.
26. Galluzzi L, Kepp O, Kroemer G. Enlightening the impact of immunogenic cell death in photodynamic cancer therapy. *EMBO J* 2012;**31**:1055−7.
27. Chen C, Ni X, Jia S, Liang Y, Wu X, Kong D, et al. Massively evoking immunogenic cell death by focused mitochondrial oxidative stress using an AIE luminogen with a twisted molecular structure. *Adv Mater* 2019;**31**:e1904914.
28. Feng B, Hou B, Xu Z, Saeed M, Yu H, Li Y. Self-amplified drug delivery with light-inducible nanocargoes to enhance cancer immunotherapy. *Adv Mater* 2019;**31**:e1902960.
29. Xu J, Xu L, Wang C, Yang R, Zhuang Q, Han X, et al. Near-infrared-triggered photodynamic therapy with multitasking upconversion nanoparticles in combination with checkpoint blockade for immunotherapy of colorectal cancer. *ACS Nano* 2017;**11**:4463−74.
30. Zorov DB, Filburn CR, Klotz LO, Zweier JL, Sollott SJ. Reactive oxygen species (ROS)-induced ROS release: a new phenomenon accompanying induction of the mitochondrial permeability transition in cardiac myocytes. *J Exp Med* 2000;**192**:1001−14.
31. Zorov DB, Juhaszova M, Sollott SJ. Mitochondrial ROS-induced ROS release: an update and review. *Biochim Biophys Acta* 2006;**1757**:509−17.
32. Feng Z, Han X, Wang H, Tang T, Xu B. Enzyme-instructed peptide assemblies selectively inhibit bone tumors. *Chem* 2019;**5**:2442−9.
33. Wang H, Feng Z, Wang Y, Zhou R, Yang Z, Xu B. Integrating enzymatic self-assembly and mitochondria targeting for selectively killing cancer cells without acquired drug resistance. *J Am Chem Soc* 2016;**138**:16046−55.
34. Du X, Zhou J, Wang H, Shi J, Kuang Y, Zeng W, et al. *In situ* generated D-peptidic nanofibrils as multifaceted apoptotic inducers to target cancer cells. *Cell Death Dis* 2017;**8**:e2614.
35. Zheng D, Chen Y, Ai S, Zhang R, Gao Z, Liang C, et al. Tandem molecular self-assembly selectively inhibits lung cancer cells by inducing endoplasmic reticulum stress. *Research (Wash DC)* 2019;**2019**:4803624.
36. Li X, Cai X, Zhang Z, Ding Y, Ma R, Huang F, et al. Mimetic heat shock protein mediated immune process to enhance cancer immunotherapy. *Nano Lett* 2020;**20**:4454−63.
37. Ren CH, Wang ZY, Zhang XL, Gao J, Gao Y, Zhang YM, et al. Construction of all-in-one peptide nanomedicine with photoacoustic imaging guided mild hyperthermia for enhanced cancer chemotherapy. *Chem Eng J* 2021;**405**:127008.
38. Wang JY, Li JQ, Xiao YM, Fu B, Qin ZH. Triphenylphosphonium (TPP)-based antioxidants: a new perspective on antioxidant design. *ChemMedChem* 2020;**15**:404−10.
39. Zielonka J, Joseph J, Sikora A, Hardy M, Ouari O, Vasquez-Vivar J, et al. Mitochondria-targeted triphenylphosphonium-based compounds: syntheses, mechanisms of action, and therapeutic and diagnostic applications. *Chem Rev* 2017;**117**:10043−120.
40. Han X, Su R, Huang X, Wang Y, Kuang X, Zhou S, et al. Triphenylphosphonium-modified mitochondria-targeted paclitaxel nanocrystals for overcoming multidrug resistance. *Asian J Pharm Sci* 2019;**14**:569−80.
41. Jeena MT, Palanikumar L, Go EM, Kim I, Kang MG, Lee S, et al. Mitochondria localization induced self-assembly of peptide amphiphiles for cellular dysfunction. *Nat Commun* 2017;**8**:26.
42. Li X, Wang Y, Wang S, Liang C, Pu G, Chen Y, et al. A strong $CD8^+$ T cell-stimulating supramolecular hydrogel. *Nanoscale* 2020;**12**:2111−7.
43. Fishman WH. Clinical and biological significance of an isozyme tumor marker—PLAP. *Clin Biochem* 1987;**20**:387−92.
44. Zhan J, Cai Y, He S, Wang L, Yang Z. Tandem molecular self-assembly in liver cancer cells. *Angew Chem Int Ed Engl* 2018;**57**:1813−6.
45. Wemeau M, Kepp O, Tesniere A, Panaretakis T, Flament C, De Botton S, et al. Calreticulin exposure on malignant blasts predicts a cellular anticancer immune response in patients with acute myeloid leukemia. *Cell Death Dis* 2010;**1**:e104.
46. Vasaturo A, Verdoes M, de Vries J, Torensma R, Figdor CG. Restoring immunosurveillance by dendritic cell vaccines and manipulation of the tumor microenvironment. *Immunobiology* 2015;**220**:243−8.
47. Tuettenberg A, Schmitt E, Knop J, Jonuleit H. Dendritic cell-based immunotherapy of malignant melanoma: success and limitations. *J Dtsch Dermatol Ges* 2007;**5**:190−6.
48. Trahtemberg U, Mevorach D. Apoptotic cells induced signaling for immune homeostasis in macrophages and dendritic cells. *Front Immunol* 2017;**8**:1356.